metals

MDPI

Article

# Synthesis of Spherical V-Nb-Mo-Ta-W High-Entropy Alloy Powder Using Hydrogen Embrittlement and Spheroidization by Thermal Plasma

**Won-Hyuk Lee [1,2], Ki Beom Park [1], Kyung-Woo Yi [2], Sung Yong Lee [1], Kwangsuk Park [1], Taeg Woo Lee [1], Tae-Wook Na [1,*] and Hyung-Ki Park [1,*]**

[1] Gangwon Regional Division, Korea Institute of Industrial Technology, Gangneung 25440, Korea; ownhug@kitech.re.kr (W.-H.L.); hope92430@kitech.re.kr (K.B.P.); sylee494@kitech.re.kr (S.Y.L.); kpark63@kitech.re.kr (K.P.); twlee@kitech.re.kr (T.W.L.)

[2] Department of Material Science and Engineering, Seoul National University, Seoul 08826, Korea; yikw@snu.ac.kr

* Correspondence: arkasa86@kitech.re.kr (T.-W.N.); mse03@kitech.re.kr (H.-K.P.); Tel.: +82-33-649-4049 (T.-W.N.); +82-33-649-4016 (H.K.P.)

Received: 16 November 2019; Accepted: 28 November 2019; Published: 1 December 2019

check for updates

**Abstract:** V-Nb-Mo-Ta-W high-entropy alloy (HEA), one of the refractory HEAs, is considered as a next-generation structural material for ultra-high temperature uses. Refractory HEAs have low castability and machinability due to their high melting temperature and low thermal conductivity. Thus, powder metallurgy becomes a promising method for fabricating components with refractory HEAs. Therefore, in this study, we fabricated spherical V-Nb-Mo-Ta-W HEA powder using hydrogen embrittlement and spheroidization by thermal plasma. The HEA ingot was prepared by vacuum arc melting and revealed to have a single body-centered cubic phase. Hydrogen embrittlement which could be achieved by annealing in a hydrogen atmosphere was introduced to get the ingot pulverized easily to a fine powder having an angular shape. Then, the powder was annealed in a vacuum atmosphere to eliminate the hydrogen from the hydrogenated HEA, resulting in a decrease in the hydrogen concentration from 0.1033 wt% to 0.0003 wt%. The angular shape of the HEA powder was turned into a spherical one by inductively-coupled thermal plasma, allowing to fabricate spherical V-Nb-Mo-Ta-W HEA powder with a $d_{50}$ value of 28.0 μm.

**Keywords:** high-entropy alloy; refractory metal; powder; hydrogen embrittlement; spheroidization; thermal plasma

## 1. Introduction

High-entropy alloys (HEAs), composed of five or more metallic elements in an equimolar or near-equimolar ratio, have been intensively studied since the first development by Yeh et al. [1]. As HEAs possess a high-entropy effect, severe lattice distortion, sluggish diffusion, and the cocktail effect, they exhibit unique properties such as high hardness [2,3], high strength [4–6], low electrical conductivity [7], low thermal conductivity [7–9], and high thermal stability [10]. So HEAs have been considered as promising candidates for high-strength alloys [11–13], corrosion-resistant alloys [14–16], wear-resistant alloys [17,18], and diffusion barriers [19,20].

There are two primary categories of HEAs: HEAs with a face-centered cubic (FCC) structure [1–7] and HEAs with a body-centered cubic (BCC) structure [21,22]. Cantor alloy, as a typical form of FCC HEA which is composed of Cr, Mn, Fe, Co, and Ni, has been studied for cryogenic alloys because the alloy has high toughness and strength at low temperature [23]. On the other hand, refractory BCC HEAs, which usually contain Ti, V, Cr, Zr, Nb, Mo, Hf, Ta, and W, were researched intensively as high-temperature alloys due to their enhanced mechanical properties at elevated temperatures [11,21]. For example, the yield strengths of Ti-Nb-Mo-Ta-W and Ti-V-Nb-Mo-Ta-W was reported to be 586 MPa and 659 MPa at 1200 °C, respectively [21]. In addition, V-Nb-Mo-Ta-W and Nb-Mo-Ta-W alloys, as reported by Senkov et al. [11], have yield strengths of 405 MPa and 477 MPa at 1600 °C, respectively.

Refractory HEAs have low castability and machinability because they have a high melting point and low thermal conductivity. Also, HEAs have low formability due to their low ductility and brittle nature. Therefore, the near-net-shape processes based on the powder metallurgy would be an effective approach in fabricating components for refractory HEAs. However, to do this, the powder for refractory HEAs needs to be fabricated. In particular, a fine spherical powder is needed for near-net-shape powder metallurgy processes, such as additive manufacturing [24] and metal powder injection molding [25]. However, fabrication processes for the spherical powder of refractory BCC HEAs have not yet been developed; conventional methods for the fabrication of spherical powder, such as gas atomization, seem not to be applicable for the refractory BCC HEAs due to their extremely high melting temperature.

Grinding could be a way of fabricating powder if an ingot is sufficiently brittle. However, The V-Nb-Mo-Ta-W HEA ingot is not brittle enough to be crushed, indicating that additional processes are needed to make it brittle. Hydrogen embrittlement is a good approach to obtain the required brittleness, which is simply achieved by exposure of metals to hydrogen atmosphere at an adequate temperature, resulting in the hydrogen-triggered ductile-to-brittle phenomenon [26]. The loss in strength of metals, when exposed to hydrogen, can be explained by the hydrogen-enhanced decohesion mechanism [26,27]. It is known that crack can be initiated and even propagated by the localized stress, induced by hydrogen absorption [28]. Among the HEAs, FCC HEAs are reported to have high hydrogen-embrittlement resistance, but BCC HEAs are not studied well yet [29–32].

Therefore, in this study, we introduced a new method to fabricate spherical V-Nb-Mo-Ta-W HEA powder, where hydrogen embrittlement and spheroidization by thermal plasma were used. In addition, we investigated the morphology, microstructure, and crystal structure of the ingot and powder.

## 2. Materials and Methods

A process was designed for the fabrication of spherical V-Nb-Mo-Ta-W HEA powder and is shown in Figure 1. The HEA ingot, with a chemical composition of 20V-20Nb-20Mo-20Ta-20W (at%), was prepared by vacuum arc remelting. The ingot was remelted five times and cast into a water-cooled copper crucible with a cylindrical shape. To homogenize the composition, the ingot was annealed at 1400 °C for 10 h in a high-purity (5 N) argon atmosphere. The chemical composition of the ingot was examined by wavelength-dispersive X-ray fluorescence spectrometry and the results are shown in Table 1.

**Table 1.** The chemical composition of each component in the VNbMoTaW HEA ingot.

| **Element** | **Ta** | **W** | **Nb** | **Mo** | **V** |
|---|---|---|---|---|---|
| Atomic% | 21.07 | 19.75 | 19.3 | 20.39 | 19.49 |

To make the ingot brittle, the ingot was heated at the rate of 10 °C/min and annealed at 600 °C for 1 h in a 100% hydrogen atmosphere. The hydrogen-annealed ingot was crushed into particles with sizes less than 1 mm by a jaw crusher. The particles were ball-milled in 1000 cc stainless steel containers using tungsten carbide balls with a 5 mm diameter as the milling media. The milling container was purged by 5 N argon and the ball-to-powder ratio was 5:1 by weight. After ball-milling for 5 h at the rotation speed of 200 rpm, the powder was sieved using a 45-µm mesh. To eliminate hydrogen, the powder was heated at the rate of 10 °C/min and annealed at 600 °C for 1 h in a high-vacuum (~$10^{-5}$ Torr) atmosphere.

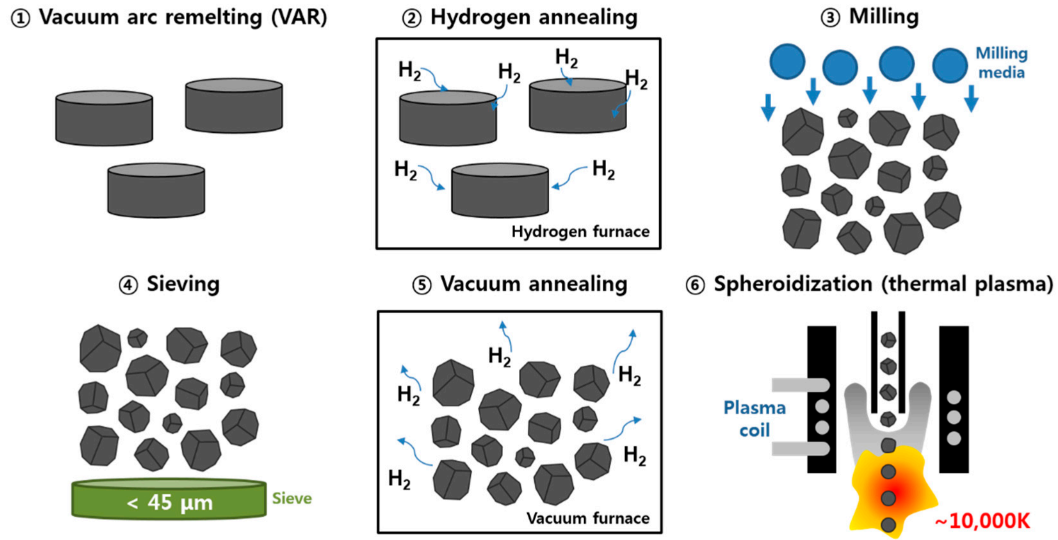

**Figure 1.** Schematic process for the fabrication of spherical V-Nb-Mo-Ta-W high-entropy alloy (HEA) powder.

The vacuum-annealed powder was spheroidized using inductively-coupled thermal plasma (PLASNIX, RFP-10). The powder was injected into a chamber with the feeding rate of 500 g/h using a vibration-type feeder. Argon gas was used as the center gas and powder-carrier gas at the flow rates of 5 and 2 slm (standard litre per minute), respectively. An argon-and-helium gas mixture, with an argon/helium ratio of 4, was injected as the sheath gas, with a flow rate of 75 slm, to protect the chamber from plasma. The pressure of the plasma chamber was set to 90 kPa during plasma treatment. The plasma power was 8 kW and the oscillation frequency was 13.56 MHz.

The shapes of the ingot before and after hydrogen annealing were observed by an optical camera. The microstructure of each sample was analyzed by a field-emission scanning electron microscope (FE-SEM) (QUANTA FEG 250, FEI, Hillsboro, OR, USA). The dendritic structures were observed by back-scattered electron (BSE) imaging and the grain boundaries were evaluated by electron backscatter diffraction (EBSD) (DigiVeiw, EDAX, Mahwah, NJ, USA). The chemical compositions of the dendritic structure in the ingot were analyzed by an energy dispersive spectrometer (EDS). The phases of the samples were analyzed by using an X-ray diffractometer (XRD) (Empyrean, Malvern Panalytical, Malvern, UK). The oxygen, nitrogen, and hydrogen concentrations were obtained by using an O/N/H analyzer (736 series, LECO, St. Joseph, MA, USA). The thickness of the dendritic structure of the spheroidized powder was about 150 nm. The chemical compositions of the dendritic structure in the spheroidized powder were analyzed by transmission electron microscopy (TEM) (JEM-2100F, JEOL, Akishima, Japan). The TEM sample was prepared by a focused ion beam (FIB) (NOVA-200 NanoLab, FEI, Hillsboro, OR, USA).

To examine the mechanical properties of the ingots before and after hydrogen annealing, compression tests were carried out with a strain rate of $2 \times 10^{-3}$ $s^{-1}$, using a universal testing machine (5982, Instron, Norwood, MA, USA). Cylindrical samples with a 4-mm diameter and 7-mm height were used for the compression tests. The Vickers hardness test was performed to evaluate the brittleness of the samples before and after hydrogen annealing using an indenter (Mitutoyo, HM-200). The indentation load for the hardness test was 2 kgf.

## 3. Results and Discussion

Figure 2a shows the V-Nb-Mo-Ta-W HEA ingot with a size of ϕ 70 mm × 20 mm H fabricated by vacuum arc remelting. The BSE image in Figure 3a shows the microstructure of the ingot. Similar to a previous report [12], the V-Nb-Mo-Ta-W ingot had a dendritic microstructure. The thickness of the dendrite arm was about 20 μm and that of the interdendritic region was about 3 μm. Figure 4 shows the EDS mapping results of the ingot. The results showed that the dendrite arm was a W- and Ta-rich phase and the interdendritic region was an Nb-, Mo-, and V-rich phase.

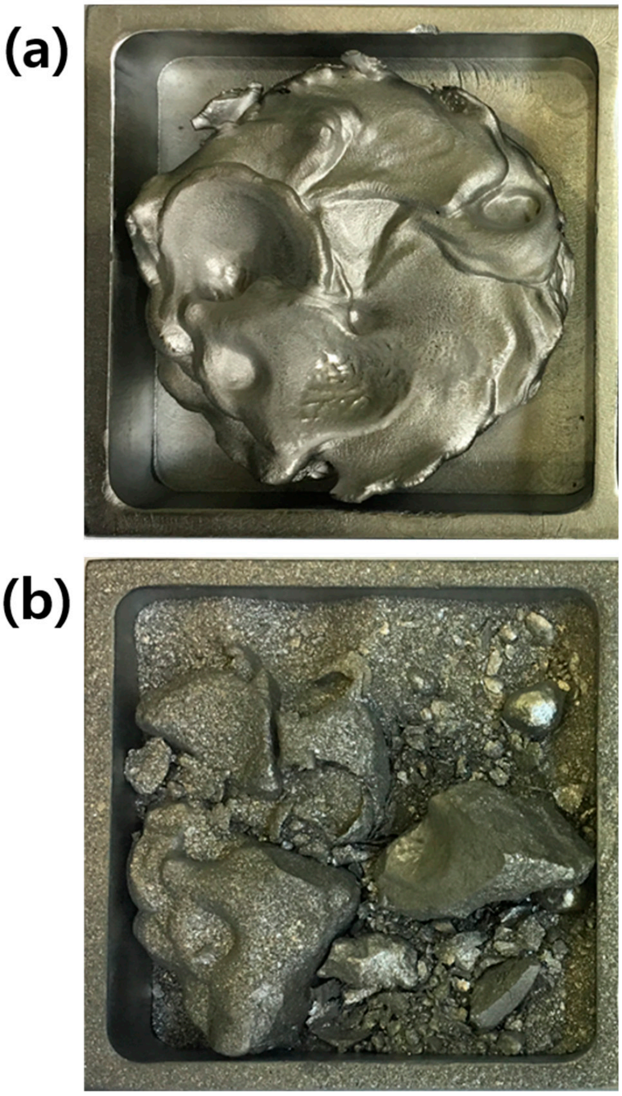

**Figure 2.** Photographs of the V-Nb-Mo-Ta-W ingot (**a**) before and (**b**) after hydrogen annealing. The ingot underwent self-crushing after hydrogen annealing.

EDS point analysis was performed for the dendrite arm; the interdendritic region and the percentages of each component are shown in Table 2. The weight percentages of V, Nb, Mo, Ta, and W at the dendrite arm were 6.00%, 14.43%, 15.60%, 30.86%, and 33.11%, respectively, while they were 18.61%, 19.12%, 17.63%, 27.46%, and 17.19%, respectively, at the interdendritic region. These results agree well with the EDS mapping results (Figure 4). It is known that a dendritic structure can be formed by the difference of the melting temperatures among the elements comprising the alloy [12]. Therefore, the W- and Ta-rich phase with a relatively high melting temperature was solidified first and then the Nb-, Mo-, and V-rich phase with a relatively low melting temperature was solidified, making the dendritic structure.

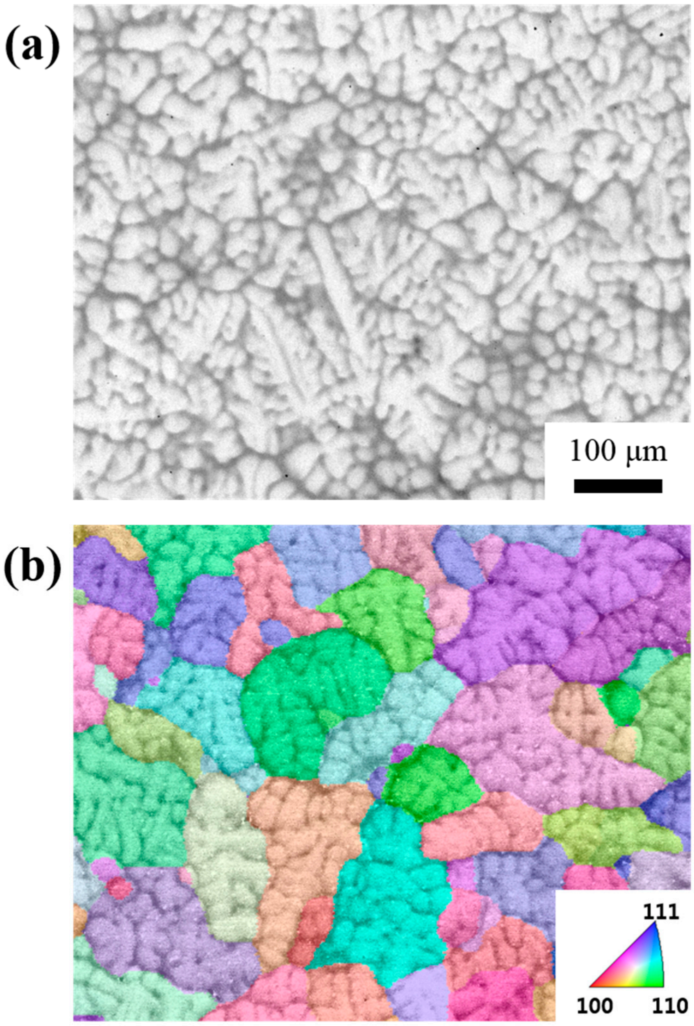

**Figure 3.** The microstructure of the V-Nb-Mo-Ta-W ingot presented in (**a**) a back-scattered electron (BSE) image and (**b**) an inverse pole figure map overlapped with the BSE image. The ingot had a dendritic microstructure with grain boundaries located at the interdendritic region.

**Table 2.** The concentrations of elements at the dendrite arm and the interdendritic region in the ingot and spheroidized powder.

| **Sample** | | | **V** | **Nb** | **Mo** | **Ta** | **W** |
|---|---|---|---|---|---|---|---|
| Ingot | Dendrite arm | wt% | 6.00 | 14.43 | 15.60 | 30.86 | 33.11 |
| | | at% | 14.97 | 19.75 | 20.68 | 21.34 | 23.26 |
| | Interdendritic region | wt% | 18.61 | 19.12 | 17.63 | 27.46 | 17.19 |
| | | at% | 36.56 | 20.59 | 18.39 | 14.95 | 9.51 |
| Spheroidized powder | Dendrite arm | wt% | 4.00 | 12.52 | 13.73 | 30.55 | 39.21 |
| | | at% | 10.62 | 18.23 | 19.35 | 22.48 | 29.31 |
| | Interdendritic region | wt% | 17.04 | 24.31 | 19.84 | 22.47 | 16.34 |
| | | at% | 32.94 | 25.76 | 20.37 | 12.03 | 8.89 |

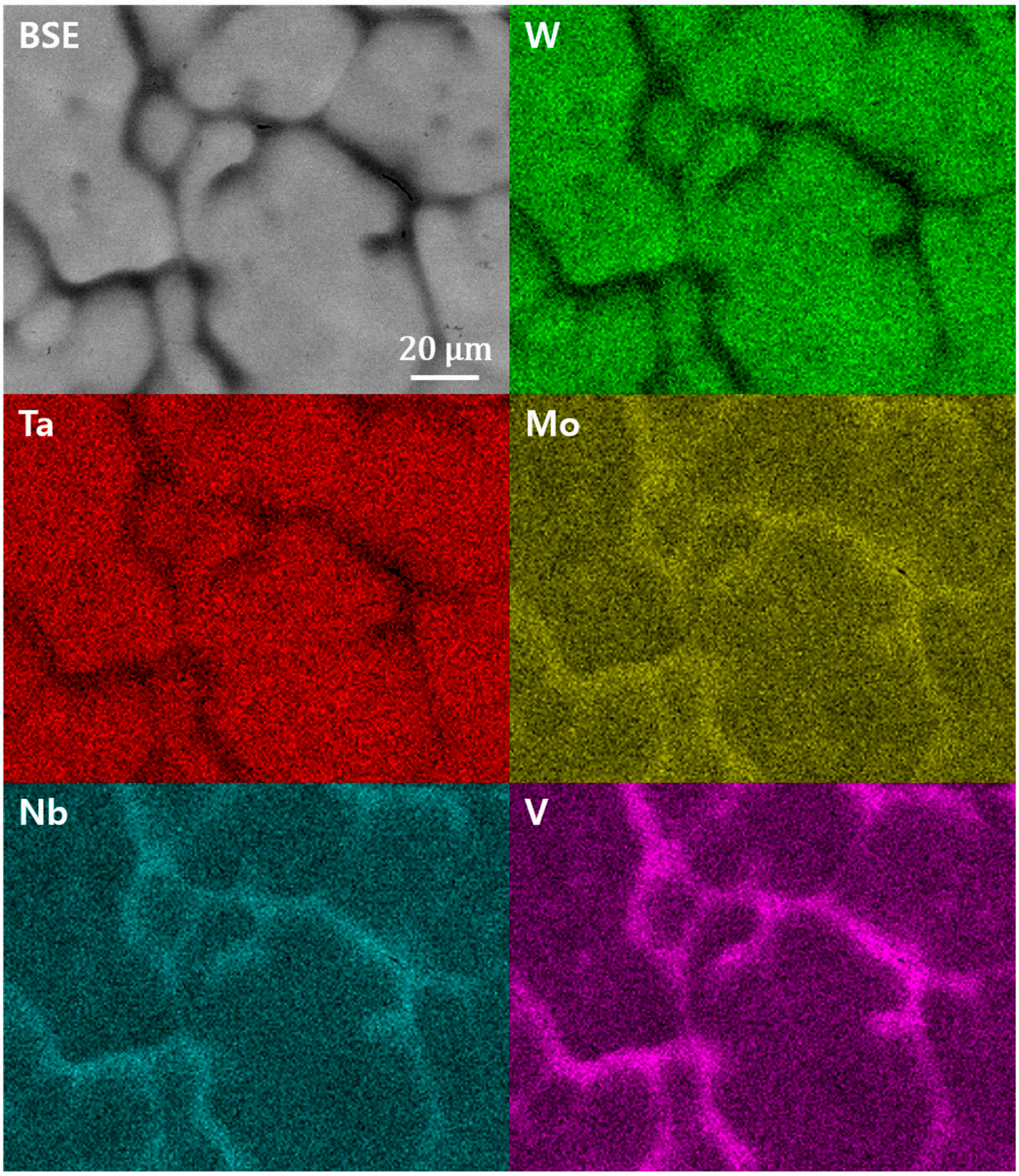

**Figure 4.** BSE image and energy dispersive spectrometer (EDS) results of the V-Nb-Mo-Ta-W ingot. Mo, Nb, and V were segregated at the interdendritic region.

To investigate the crystal structure, the ingot was analyzed by an XRD. As shown in the XRD results in Figure 5a, the XRD pattern of the ingot was matched with the single BCC phase and no other peaks of intermetallic compounds were detected. This result means that both the dendrite arm with bright contrast and the interdendritic region with dark contrast (Figure 4) had a BCC crystal structure. EBSD analysis was performed to investigate the crystallographic orientation of the dendrite arm and interdendritic regions. Figure 3b shows the inverse pole figure map overlapped with the BSE image. As shown in Figure 3b, the grain boundaries existed in the interdendritic region and the other interdendritic region without grain boundaries had the same crystallographic orientation as the nearby dendrite arm.

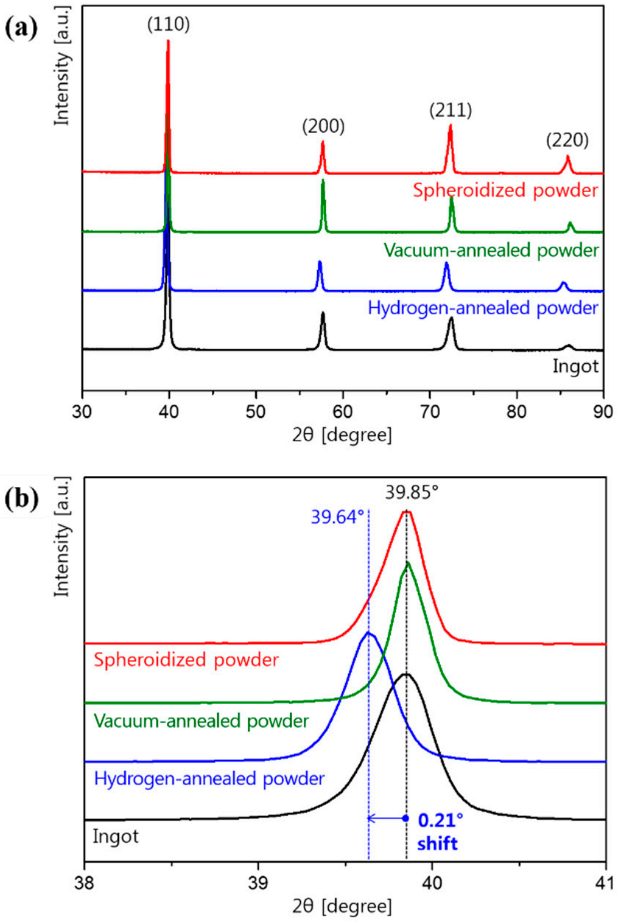

**Figure 5.** XRD results of each sample with 2θ ranges of (**a**) 30–90° and (**b**) 38–41°. The 2θ position of the (110) peak was shifted by 0.21° to a lower angle after hydrogen annealing and it returned to the original value after vacuum annealing.

In the XRD results of the ingot, the 2θ angle of (110) peaks was 39.85° with a d-spacing of 2.260 Å and the lattice parameter was calculated to be 3.197 Å. The lattice parameters of V, Nb, Mo, Ta, and W pure metals are 3.024 Å, 3.300 Å, 3.147 Å, 3.303 Å, and 3.165 Å, respectively. The average lattice parameter of the elements is 3.188 Å, which is smaller than the obtained lattice parameter of 3.197 Å. By converting the weight percentages to the atomic percentages, the atomic percentages of V, Nb, Mo, Ta, and W at the dendrite arm were determined to be 14.97%, 19.75%, 20.68%, 21.34%, and 23.26%, respectively.

Based on the lattice parameter and atomic concentrations of elements comprising the phase, the lattice parameter of the dendrite arm could be calculated using the following equation:

$$a_{\mathrm{lat}} = 2 \cdot s_{\mathrm{ave}} / (3)^{\frac{1}{2}} \tag{1}$$

where $a_{\mathrm{lat}}$ is the lattice parameter of the BCC structure and $s_{\mathrm{ave}}$ is the average of interatomic spacing. The average interatomic spacing can be predicted by the following equation [33]:

$$\mathrm{s_{ave}} = \sum \mathrm{s_{ij}.c_i.c_j} \tag{2}$$

where $s_{ij}$ is the interatomic spacing between atoms *i* and *j*, and $\mathrm{c_i}$ and $\mathrm{c_j}$ are the concentrations of atoms *i* and *j*, respectively. The interatomic spacing between two atoms is approximately similar to the average of interatomic spacing between the same atoms. Based on this assumption and Equations (1) and (2), the lattice parameter of the dendrite arm can be predicted to be 3.196 Å, which is very similar to the lattice parameter obtained in the experiment.

To make V-Nb-Mo-Ta-W HEA brittle, the ingot was annealed in a hydrogen atmosphere. Hydride-forming metals, such as V, Nb, and Ta become brittle and fracture during annealing in a hydrogen atmosphere, which is known as hydrogen embrittlement [34,35]. Though Mo and W do not form metal hydrides, V-Nb-Mo-Ta-W HEA has the potential to have a brittle nature after hydrogen annealing because of V, Nb, and Ta. Figure 2b shows a photograph of the HEA ingot obtained after hydrogen annealing. As shown in Figure 2b, the ingot was self-crushed during hydrogen annealing.

To investigate the reason for the self-crushing during hydrogen annealing, the O, N, and H concentrations and XRD patterns of the ingot before and after hydrogen annealing were investigated. Table 3 shows the results of the O/N/H analysis. The oxygen, nitrogen, and hydrogen concentrations of the ingot were 0.065 wt%, 0.004 wt%, and 0.0009 wt%, respectively. After hydrogen annealing, the oxygen, nitrogen, and hydrogen concentrations became 0.066 wt%, 0.011 wt%, and 0.1033 wt%, respectively, demonstrating a drastically-increased hydrogen concentration. The hydrogen concentration of 0.1033 wt% corresponds to a hydrogen concentration of 11.0634 at%, which indicates that a hydrogen atom exists per about 4.5 unit cells.

**Table 3.** The weight and atomic percentages of oxygen, nitrogen, and hydrogen in each sample.

| Sample | Composition | Oxygen | Nitrogen | Hydrogen |
|---|---|---|---|---|
| Ingot | wt% | 0.065 | 0.004 | 0.0009 |
| | at% | 0.488 | 0.034 | 0.1074 |
| Hydrogen-annealed powder | wt% | 0.066 | 0.011 | 0.1033 |
| | at% | 0.442 | 0.084 | 11.0634 |
| Vacuum-annealed powder | wt% | 0.067 | 0.004 | 0.0002 |
| | at% | 0.504 | 0.034 | 0.0241 |
| Spheroidized powder | wt% | 0.042 | 0.005 | 0.0003 |
| | at% | 0.316 | 0.043 | 0.0359 |

According to the XRD results shown in Figure 5, the sample after hydrogen annealing still had a BCC structure but the XRD peak positions were shifted to the left. This result means that the lattice parameter increased after hydrogen annealing. As shown in Figure 5b, the 2θ position of the (110) peak was shifted from 39.85° to 39.64°, increasing the lattice parameter from 3.197 Å to 3.213 Å. The hydrogen concentrations and XRD patterns of the ingot before and after annealing indicate that the hydrogen penetrated into the HEA ingot, extended the lattice during hydrogen annealing, and induced self-crushing by the local volume change.

To investigate the toughness of the ingot before and after hydrogen annealing, compression and indentation tests were performed on the ingots before and after hydrogen annealing. Figure 6a,b shows the results of the compression and indentation tests, respectively. For the ingot before hydrogen annealing, the maximum compressive stress was 1884 MPa and the strain at fracture was 5.1%. On the other hand, the maximum compressive stress and the strain at fracture of the ingot after hydrogen annealing decreased to 439 MPa and 3.1%, respectively. The toughness, which is the area of the curve in Figure 6a, was reduced by about 86% after hydrogen annealing. This means that only 14% of the energy for crushing the ingot was needed to crush the hydrogen-annealed ingot.

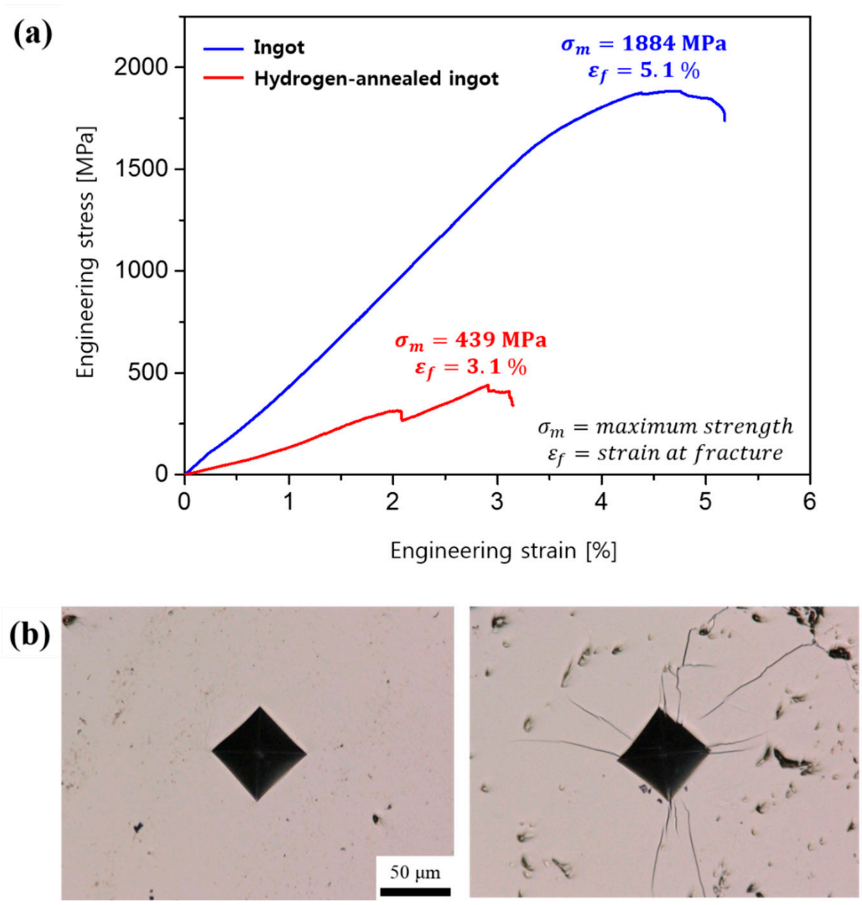

**Figure 6.** (**a**) Compression test and (**b**) indentation test of the ingot before and after hydrogen annealing. In (**b**), the left and right figures show the indentation results of the ingot before and after hydrogen annealing, respectively.

Figure 6b shows the images of the indentation test where the left and right figures are the indentation results of the ingot before and after hydrogen annealing, respectively. As shown in the indentation result of the ingot before annealing, no cracks were observed near the indentation mark. However, the hydrogen-annealed ingot became brittle so that many cracks appeared near the indentation marks after indenting, indicating that a simple milling method could be appreciable for powder fabrication. Based on the hydrogen-enhanced decohesion mechanism, the absorbed hydrogen causes not only a decrease in bonding strength of the lattice but an increase in brittleness as well, as a result of the accumulation of the absorbed hydrogen atoms at crack tips [26–28]. As a result, the absorbed hydrogen gets the BCC HEA ingot weakened to pulverization [36].

The ingot after hydrogen annealing was pulverized easily by jaw crushing and ball-milling because of its brittle nature. After sieving, the powder was annealed in a vacuum atmosphere to remove hydrogen from the powder. Figure 7 shows the morphologies of the vacuum-annealed powder. The powder has angular shapes, similar to Nb and Ti powder fabricated by the hydrogenation-dehydrogenation reaction [35,37,38]. As shown in Figure 5b, the 2θ position of the (110) XRD peak returned from 39.64° to 39.86° after vacuum annealing. The oxygen, nitrogen, and hydrogen concentrations of the vacuum-annealed powder were 0.067 wt%, 0.004 wt%, and 0.0002 wt%, respectively, which are similar to those of the ingot. According to these results, hydrogen present in the HEA powder after milling was successfully eliminated by vacuum annealing.

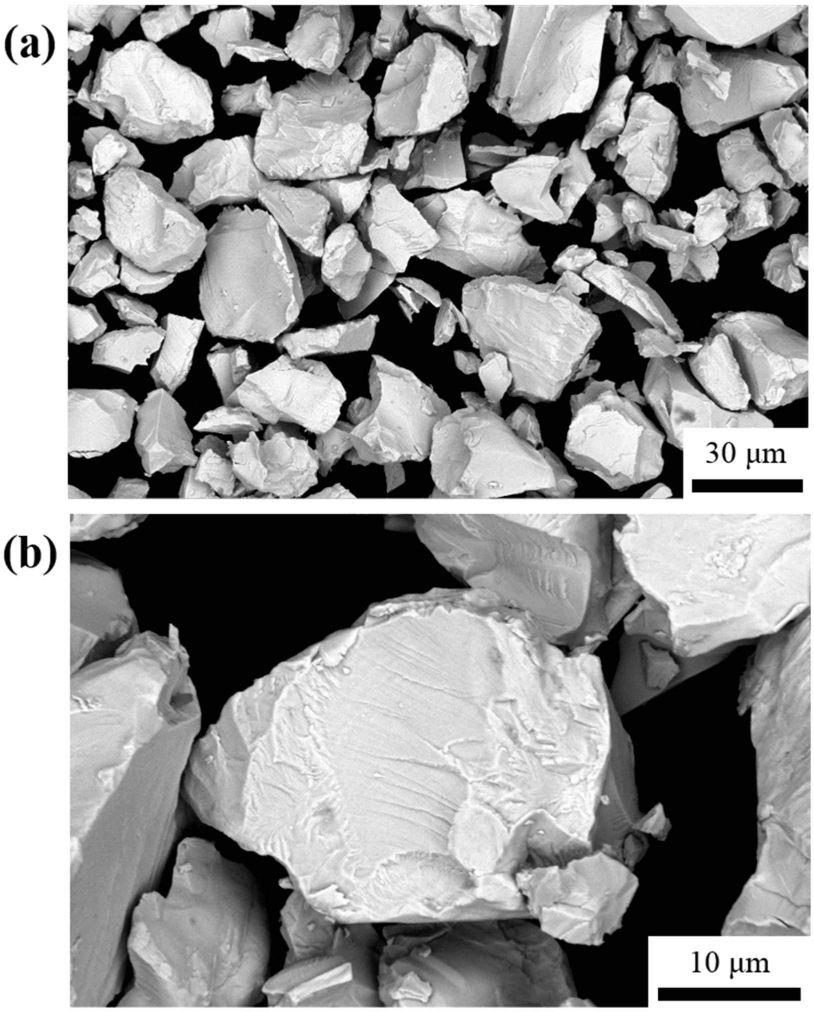

**Figure 7.** Morphologies of the vacuum-annealed V-Nb-Mo-Ta-W powder observed by SEM at (**a**) low and (**b**) high magnification. The powder had an angular shape.

The vacuum-annealed powder was spheroidized by inductively-coupled thermal plasma. The maximum temperature in the thermal plasma chamber can reach 10,000 K [39]. The HEA powder can be fully melted and spheroidized to reduce the surface area due to the surface tension effect. Figure 8 shows the morphologies of the spheroidized powder. As shown in Figure 8, the HEA powder was successfully spheroidized and the $d_{10}$, $d_{50}$, and $d_{90}$ values of the spherical powder were 15.0, 28.0, and 43.8 μm, respectively.

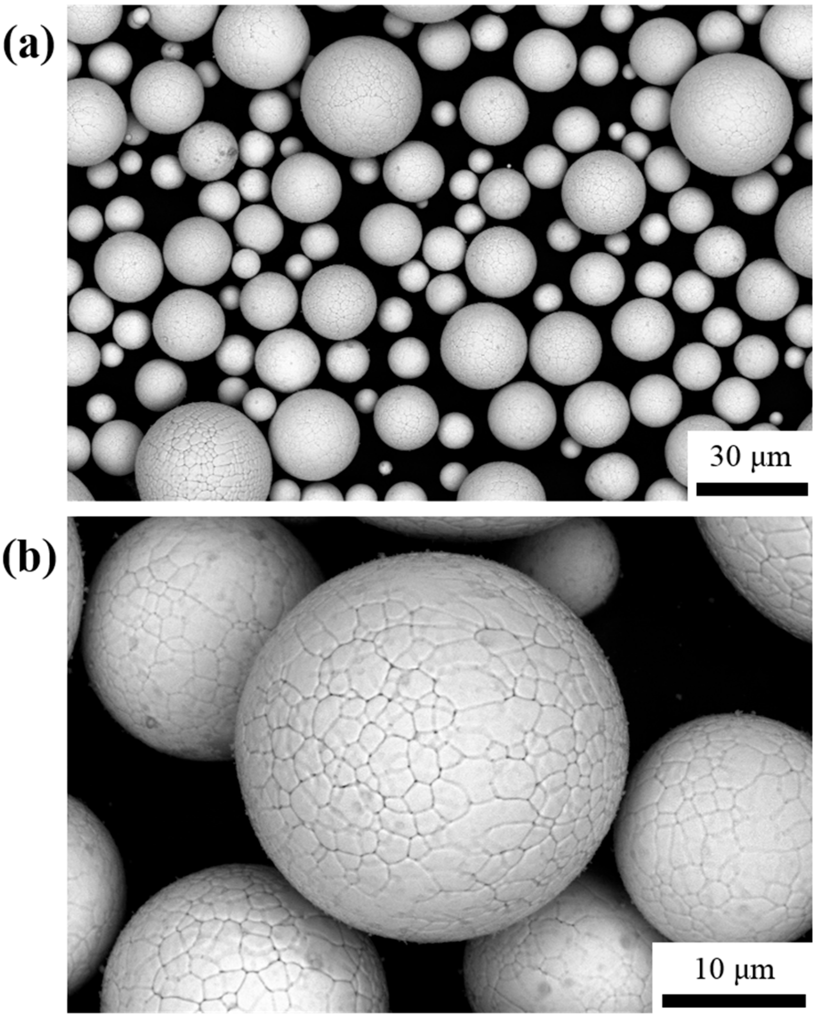

**Figure 8.** Morphologies of the spheroidized V-Nb-Mo-Ta-W powder observed by SEM at (**a**) low and (**b**) high magnification. The powder had a spherical shape.

The oxygen, nitrogen, and hydrogen concentrations of the spheroidized HEA powder were 0.042 wt%, 0.005 wt%, and 0.0003 wt%, respectively. The oxygen concentration of the vacuum-annealed powder was 0.067 wt% and it decreased to 0.042 wt% after thermal plasma treatment. If oxidation occurs during the thermal plasma treatment, the oxygen concentration of powder should be increased or at least maintained. However, as oxidation is an exothermal reaction, the driving force of oxidation decreases with temperature and as a result, the atmosphere of the thermal plasma treatment could be changed to a reducing atmosphere due to the extremely high temperature, as high as 10,000 K, leading to the reduction of the oxygen content.

To investigate the microstructure of the spheroidized powder, the cross-sections of the spherical powder were investigated by SEM and the results are shown in Figure 9. To observe the cross-section of powder, the spheroidized powder was hot-mounted with conductive carbon resin and polished. In Figure 9a, the BSE image of the cross-section clearly shows a fine dendritic structure formed in the powder after spheroidization. The thickness of the dendrite arm ranged from 1 to 10 μm and that of the interdendritic region was less than 0.5 μm, which are much smaller than those of the ingot. Since the thickness of the dendrite arm decreases with increasing solidification rate [40], the fine dendritic structure of the spheroidized powder could be a result of rapid solidification during the plasma treatment. As shown in Figure 5a, the XRD pattern of the spheroidized powder was similar to that of the vacuum-annealed powder without any phase transformation. Figure 9b–d shows the

IPF maps of other spheroidized powders observed by EBSD in the cross-sectional view. The points with a confidence index value under 0.1 were colored black to eliminate the region of the resin. As shown in Figure 9b–d, all of the observed particles had only one crystallographic orientation, being a single crystal.

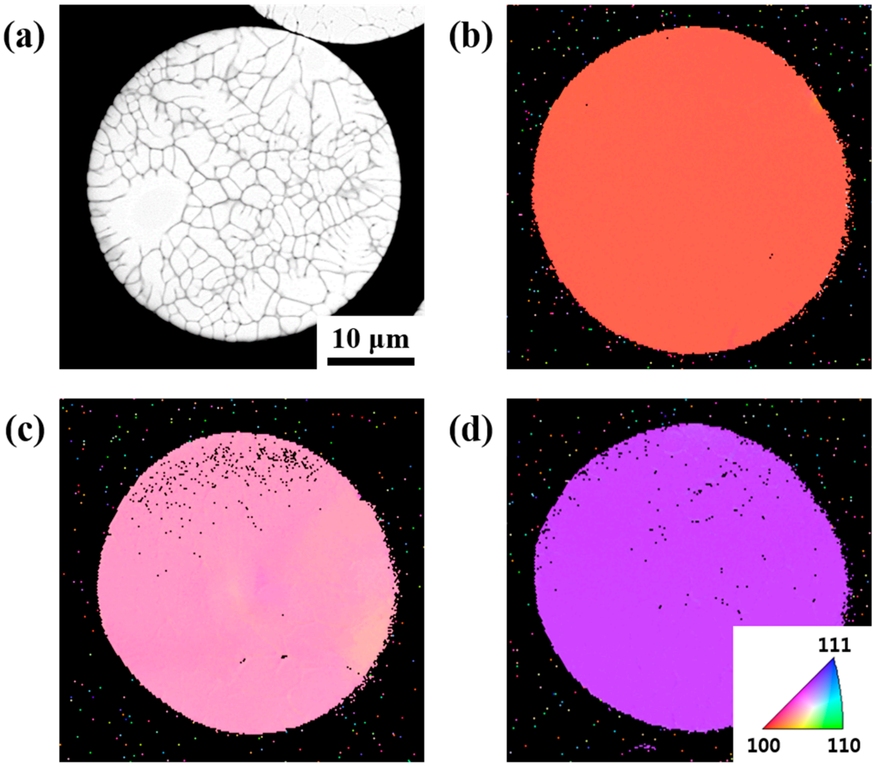

**Figure 9.** (**a**) SEM image and (**b**–**d**) inverse pole figure(IPF) maps of the spheroidized V-Nb-Mo-Ta-W powder particles. The spheroidized powder shows a single crystal, as well as a dendritic structure.

To investigate the difference between the dendrite arm and the interdendritic region, a sample near the interdendritic region taken by FIB was observed by TEM, as shown in Figure 10. Figure 10a,b shows the location of the line scanning and the results of line scanning, respectively. Similarly to the dendrite structure of the ingot, the dendrite arm consisted of a W- and Ta-rich phase and the interdendritic region was a V- and Nb-rich phase. As shown in Table 2, the atomic percentages of V, Nb, Mo, Ta, and W at the dendrite arm were 10.62%, 18.23%, 19.35%, 22.48%, and 29.31%, respectively and those at the interdendritic region were 32.94%, 25.76%, 20.37%, 12.03%, and 8.89%, respectively.

Based on the concentration of each element, the lattice parameters of the dendrite arm and the interdendritic region in the spheroidized powder can be predicted to be 3.202 and 3.166 Å, respectively, using Equation (2). Based on the prediction, the (110) d-spacings of the dendrite arm and the interdendritic region could be calculated to be 2.264 and 2.239 Å, respectively. After spheroidization, the 2θ position of the (110) XRD peak was 2θ = 39.83° (Figure 5). The XRD result indicates that the (110) d-spacing of the spheroidized powder was 2.262 Å, which is similar to the calculated (110) d-spacing value of the dendrite arm.

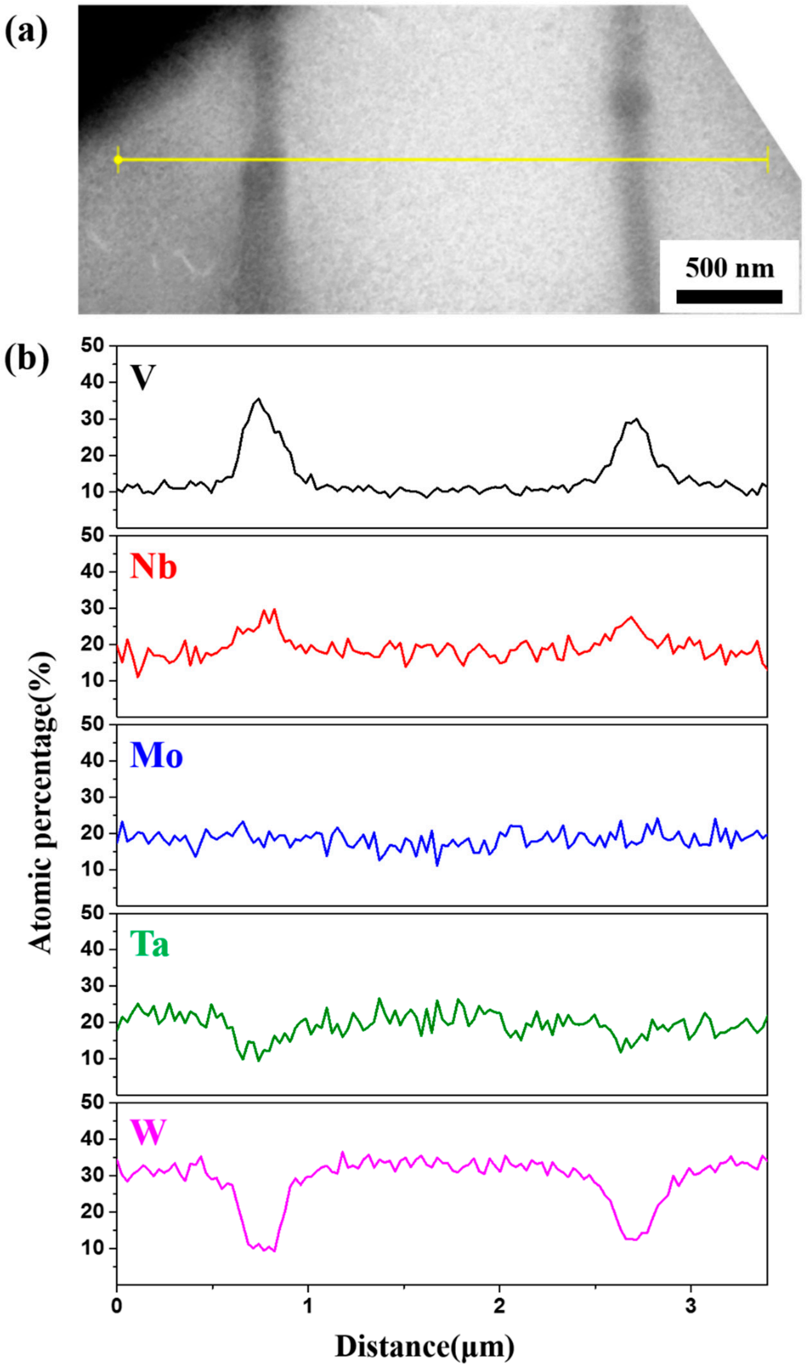

**Figure 10.** Line scanning results observed by TEM near the interdendritic region: (**a**) TEM image representing the scanning location and (**b**) concentration of each element along the location. V and Nb were segregated at the interdendritic region.

## 4. Conclusions

The spherical refractory BCC HEA powder with a chemical composition of 20V-20Nb-20Mo-20Ta-20W (at%) was successfully fabricated through the combination of hydrogenation and spheroidization processes. During hydrogen annealing, the ingot underwent self-crushing as a result of the hydrogen embrittlement, where the hydrogen concentration was increased from 0.0009 wt% up to 0.1033 wt%. The brittle characteristic of the hydrogen-annealed ingot made it possible to to be pulverized further by only the ball-milling process. The angular shape of the ball-milled powder could be spheroidized by the vacuum annealing, followed by the thermal plasma process. The resulting powder showed the spherical shape and its size was revealed to be 15.0, 28.0, and 43.8 µm in terms of $d_{10}$, $d_{50}$, and $d_{90}$. As in the case of the ingot, the spherical powder also had a dendrite structure but showed a very narrow interdendritic distance, as short as 0.5 µm, which would be ascribed to the rapid solidification. The compositional analysis revealed that the dendrite arm was a Ta- and W-rich region with a lattice parameter of 3.202 Å, whereas the interdendritic region was an Nb- and V-rich region with a lattice parameter of 3.166 Å.

**Author Contributions:** Conceptualization, W.-H.L. and H.-K.P.; methodology, K.B.P. and K.-W.Y.; investigation, S.Y.L., K.P. and T.W.L.; writing—original draft preparation, T.-W.N.

**Funding:** This study was conducted with the support of the Korea Institute of Industrial Technology (KITECH EO-19-0067). Kyung-Woo Yi acknowledges the support of Seoul National University.

**Acknowledgments:** This study has been conducted with the support of the Korea Institute of Industrial Technology (KITECH EO-19-0067).

**Conflicts of Interest:** The authors declare no conflict of interest.

## References

1. Yeh, J.W.; Chen, S.K.; Lin, S.J.; Gan, J.Y.; Chin, T.S.; Shun, T.T.; Tsau, C.H.; Chang, S.Y. Nanostructured high-entropy alloys with multiple principal elements: Novel alloy design concepts and outcomes. *Adv. Eng. Mater.* **2004**, *6*, 299–303. [CrossRef]
2. Youssef, K.M.; Zaddach, A.J.; Niu, C.; Irving, D.L.; Koch, C.C. A novel low-density, high-hardness, high-entropy alloy with close-packed single-phase nanocrystalline structures. *Mater. Res. Lett.* **2015**, *3*, 95–99. [CrossRef]
3. Yu, P.F.; Zhang, L.J.; Cheng, H.; Zhang, H.; Ma, M.Z.; Li, Y.C.; Li, G.; Liaw, P.K.; Liu, R.P. The high-entropy alloys with high hardness and soft magnetic property prepared by mechanical alloying and high-pressure sintering. *Intermetallics* **2016**, *70*, 82–87. [CrossRef]
4. Yeh, J.; Chen, S.; Gan, J.; Lin, S.; Chin, T. Formation of simple crystal structures in Cu-Co-Ni-Cr-Al-Fe-Ti-V alloys with multiprincipal metallic elements. *Metall. Mater. Trans. A* **2010**, *35*, 2533–2536. [CrossRef]
5. Zhou, Y.J.; Zhang, Y.; Wang, Y.L.; Chen, G.L. Solid solution alloys of $AlCoCrFeNiTi_x$ with excellent room-temperature. *Appl. Phys. Lett.* **2014**, *90*, 181904. [CrossRef]
6. Fu, Z.; Chen, W.; Fang, S.; Zhang, D.; Xiao, H.; Zhu, D. Alloying behavior and deformation twinning in a CoNiFeCrAl0. 6Ti0. 4 high entropy alloy processed by spark plasma sintering. *J. Alloys Compd.* **2013**, *553*, 316–323. [CrossRef]
7. Chou, H.P.; Chang, Y.S.; Chen, S.K.; Yeh, J.W. Microstructure, thermophysical and electrical properties in $Al_xCoCrFeNi$ ($0 \leq x \leq 2$) high-entropy alloys. *Mater. Sci. Eng. B.* **2009**, *163*, 184–189. [CrossRef]
8. Fan, Z.; Wang, H.; Wu, Y.; Liu, X.; Lu, Z. Thermoelectric performance of PbSnTeSe high-entropy alloys. *Mater. Res. Lett.* **2017**, *5*, 187–194. [CrossRef]
9. Wu, W.H.; Yang, C.C.; Yeh, L.W. Industrial development of high-entropy alloys. *Ann. Chim. Des Mater.* **2006**, *31*, 737–747. [CrossRef]
10. Schuh, B.; Mendez-Martin, F.; Völker, B.; George, E.P.; Clemens, H.; Pippan, R.; Hohenwarter, A. Mechanical properties, microstructure and thermal stability of a nanocrystalline CoCrFeMnNi high-entropy alloy after severe plastic deformation. *Acta Mater.* **2015**, *96*, 258–268. [CrossRef]
11. Senkov, O.N.; Wilks, G.B.; Scott, J.M.; Miracle, D.B. Mechanical properties of $Nb_{25}Mo_{25}Ta_{25}W_{25}$ and $V_{20}Nb_{20}Mo_{20}Ta_{20}W_{20}$ refractory high entropy alloys. *Intermetallics* **2011**, *19*, 698–706. [CrossRef]
12. Senkov, O.N.; Wilks, G.B.; Miracle, D.B.; Chuang, C.P.; Liaw, P.K. Refractory high-entropy alloys. *Intermetallics* **2010**, *18*, 1758–1765. [CrossRef]
13. Stepanov, N.D.; Shaysultanov, D.G.; Salishchev, G.A.; Tikhonovsky, M.A. Structure and mechanical properties of a light-weight AlNbTiV high entropy alloy. *Mater. Lett.* **2015**, *142*, 153–155. [CrossRef]
14. Chen, Y.Y.; Duval, T.; Hung, U.D.; Yeh, J.W.; Shih, H.C. Microstructure and electrochemical properties of high entropy alloys—A comparison with type-304 stainless steel. *Corros. Sci.* **2005**, *47*, 2257–2279. [CrossRef]
15. Hsu, Y.J.; Chiang, W.C.; Wu, J.K. Corrosion behavior of $FeCoNiCrCu_x$ high-entropy alloys in 3.5% sodium chloride solution. *Mater. Chem. Phys.* **2005**, *92*, 112–117. [CrossRef]

16. Shi, Y.; Yang, B.; Liaw, P. Corrosion-resistant high-entropy alloys: A review. *Metals* **2017**, *7*, 43. [CrossRef]
17. Hsu, C.Y.; Yeh, J.W.; Chen, S.K.; Shun, T.T. Wear resistance and high-temperature compression strength of Fcc CuCoNiCrAl$_{0.5}$Fe alloy with boron addition. *Metall. Mater. Trans. A* **2004**, *35*, 1465–1469. [CrossRef]
18. Chuang, M.H.; Tsai, M.H.; Wang, W.R.; Lin, S.J.; Yeh, J.W. Microstructure and wear behavior of Al$_x$Co$_{1.5}$CrFeNi$_{1.5}$Tiy high-entropy alloys. *Acta Mater.* **2011**, *59*, 6308–6317. [CrossRef]
19. Tsai, M.H.; Yeh, J.W.; Gan, J.Y. Diffusion barrier properties of AlMoNbSiTaTiVZr high-entropy alloy layer between copper and silicon. *Thin Solid Films* **2008**, *516*, 5527–5530. [CrossRef]
20. Chang, S.Y.; Wang, C.Y.; Chen, M.K.; Li, C.E. Ru incorporation on marked enhancement of diffusion resistance of multi-component alloy barrier layers. *J. Alloys Compd.* **2011**, *509*, L85–L89. [CrossRef]
21. Han, Z.D.; Chen, N.; Zhao, S.F.; Fan, L.W.; Yang, G.N.; Shao, Y.; Yao, K.F. Effect of Ti additions on mechanical properties of NbMoTaW and VNbMoTaW refractory high entropy alloys. *Intermetallics* **2017**, *84*, 153–157. [CrossRef]
22. Xin, S.W.; Zhang, M.; Yang, T.T.; Zhao, Y.Y.; Sun, B.R.; Shen, T.D. Ultrahard bulk nanocrystalline VNbMoTaW high-entropy alloy. *J. Alloys Compd.* **2018**, *769*, 597–604. [CrossRef]
23. Nam, H.; Park, C.; Kim, C.; Kim, H.; Kang, N. Effect of post weld heat treatment on weldability of high entropy alloy welds. *Sci. Technol. Weld. Join.* **2018**, *23*, 420–427. [CrossRef]
24. Thompson, S.M.; Bian, L.; Shamsaei, N.; Yadollahi, A. An overview of Direct Laser Deposition for additive manufacturing; Part I: Transport phenomena, modeling and diagnostics. *Addit. Manuf.* **2015**, *8*, 36–62. [CrossRef]
25. Todd, I.; Sidambe, A.T. Developments in metal injection moulding (MIM). In *Advances in Powder Metallurgy*; Woodhead Publishing: Sawston, UK, 2013; pp. 109–146.
26. Robertson, I.M.; Sofronis, P.; Nagao, A.; Martin, M.L.; Wang, S.; Gross, D.W.; Nygren, K.E. Hydrogen embrittlement understood. *Metall. Mater. Trans. A* **2015**, *46*, 2323–2341. [CrossRef]
27. Popov, B.N.; Lee, J.W.; Djukic, M.B. Hydrogen permeation and hydrogen-induced cracking. In *Handbook of Environmental Degradation of Materials*; William Andrew Publishing: Norwich, NY, USA, 2018; pp. 133–162.
28. Djukic, M.B.; Bakic, G.M.; Zeravcic, V.S.; Sedmak, A.; Rajicic, B. The synergistic action and interplay of hydrogen embrittlement mechanisms in steels and iron: localized plasticity and decohesion. *Eng. Fract. Mech.* **2019**, *216*, 106528. [CrossRef]
29. Ichii, K.; Koyama, M.; Tasan, C.C.; Tsuzaki, K. Comparative study of hydrogen embrittlement in stable and metastable high-entropy alloys. *Scr. Mater.* **2018**, *150*, 74–77. [CrossRef]
30. Zhao, Y.K.; Lee, D.H.; Seok, M.Y.; Lee, J.A.; Phaniraj, M.P.; Suh, J.Y.; Ha, H.Y.; Kim, J.Y.; Ramamurty, U.; Jang, J.I. Resistance of CoCrFeMnNi high-entropy alloy to gaseous hydrogen embrittlement. *Scr. Mater.* **2017**, *135*, 54–58. [CrossRef]
31. Nygren, K.E.; Wang, S.; Bertsch, K.M.; Bei, H.B.; Nagao, A.; Robertson, I.M. Hydrogen embrittlement of the equi-molar FeNiCoCr alloy. *Acta Mater.* **2018**, *157*, 218–227. [CrossRef]
32. Luo, H.; Li, Z.M.; Lu, W.J.; Ponge, D.; Raabe, D. Hydrogen embrittlement of an interstitial equimolar high-entropy alloy. *Corros. Sci.* **2018**, *136*, 403–408. [CrossRef]
33. Moreen, H.A.; Taggart, R.; Polonis, D.H. A model for the prediction of lattice parameters of solid solutions. *Metall. Trans.* **1971**, *2*, 265–268. [CrossRef]
34. Owen, C.V.; Scott, T.E. Relation between hydrogen embrittlement and the formation of hydride in the group V transition metals. *Metall. Mater. Trans. B* **1972**, *3*, 1715–1726. [CrossRef]
35. Park, K.B.; Park, J.M.; Choi, J.; Kang, J.-W.; Lee, S.Y.; Park, K.; Lee, T.-W.; Na, T.-W.; Park, H.-K. Preparation of Nb-silicide based alloy powder by hydrogenation-dehydrogenation reaction. *Int. J. Refract. Met. Hard Mater.* **2018**, *76*, 180–184. [CrossRef]
36. Cotterill, P. The hydrogen embrittlement of metals. *Prog. Mater. Sci.* **1961**, *9*, 205–301. [CrossRef]
37. Azevedo, C.R.F.; Rodrigues, D.; Neto, F.B. Ti-Al-V powder metallurgy (PM) via the hydrogenation–dehydrogenation (HDH) process. *J. Alloys Compd.* **2003**, *353*, 217–227. [CrossRef]
38. Oh, J.M.; Roh, K.M.; Lee, B.K.; Suh, C.Y.; Kim, W.; Kwon, H.; Lim, J.W. Preparation of low oxygen content alloy powder from Ti binary alloy scrap by hydrogenation-dehydrogenation and deoxidation process. *J. Alloys Compd.* **2014**, *593*, 61–66. [CrossRef]

39. Boulos, M.I. The role of transport phenomena and modeling in the development of thermal plasma technology. *Plasma Chem. Plasma Process.* **2016**, *36*, 3–28. [CrossRef]
40. Grant, N.J. Rapid solidification of metallic particulates. *JOM* **1983**, *35*, 20–27. [CrossRef]